Microscale plasma actuators for improved thrust density

Chin-Cheng Wang and Subrata Roy[a)]
Department of Mechanical and Aerospace Engineering, Computational Plasma Dynamics Laboratory and Test Facility, Applied Physics Research Group, University of Florida, Gainesville, Florida 32611, USA

(Received 10 March 2009; accepted 24 May 2009; published online 10 July 2009)

We present a study of the dielectric barrier discharge (DBD) plasma actuators for microscale applications. Traditional macroscale DBD actuators suffer from relatively small actuation effect as characterized by small induced force density and resulting flow velocity. As a remedy we propose microscale plasma actuators that may induce orders of magnitude higher force density. We study the physics of such actuation using a multiscale ionized gas flow code based on the high-fidelity finite-element procedure. First, a two-dimensional volume discharge with nitrogen as a working gas is investigated using a first-principles approach solving coupled system of hydrodynamic plasma equations and Poisson equation for ion density, electron density, and electric field distribution. The quasi-neutral plasma and the sheath regions are identified. As the gap between electrodes is reduced, the sheath structure dominates the plasma region. Second, we simulate a first generation plasma micropump. We solve multiscale plasma-gas interaction inside a two-dimensional cross section of the microscale pump geometry. The result shows that a reasonable mass flow rate can be pumped using a set of small active electrodes. © *2009 American Institute of Physics*.
[DOI: 10.1063/1.3160304]

I. INTRODUCTION

The plasma that has been used for the flow actuation at atmospheric pressure is a weakly ionized gas, where the ions are often near the ambient pressure and temperature. The dielectric barrier discharge (DBD) plasma actuator for flow actuation shown in Fig. 1 needs an asymmetric configuration of electrodes differentially powered at a radio frequency (rf). This configuration creates an electrohydrodynamic (EHD) force generated by the interaction of the charged particles with an external electric circuit. Recently, researchers have widely investigated application of EHD force for drag reduction behind the airfoils and fuselages at a high angle-of-attack.[1–3] However, the primary weakness of traditional DBD actuators is the relatively small flow actuation effect. It has been proven to be quite effective only at low speeds (10–30 m/s). In order to remedy this weakness, microscale discharge is proposed to increase the higher EHD force density with lower power consumption.

Generating a plasma discharge at atmospheric pressures using several microns gap is a promising approach. Such gap lowers breakdown voltage requirement (hence, lowers power consumption) to drive the discharge. Microscale discharge has been studied for many applications over the past decade. Such applications include NO_x and SO_x remediation, volatile organic compounds destruction, ozone generation, excimer formation as UV radiation sources, materials processing, and surface modification as plasma reactors.[4]

The size of an actuator is ultimately limited by the breakdown voltage of the working material. Electrical breakdown is the process by which a nonconducting material transforms into a conductor as a result of a sufficiently strong electric field. This occurs when the applied voltage at least equals to the breakdown voltage. The breakdown characteristic of a gap is a function of the product of the gas pressure p and the gap length d based on Paschen's law. Several studies have been reported in the literature documenting electrical breakdown voltage varying from 300 to 750 V in microscale gap ($\sim 10-10^2$ μm).[5–8] Torres and Dhariwal[7] and Germer[8] showed that Paschen's law was not valid for gaps of less than 5 μm between electrodes. The deviation of Paschen's curve has been conjectured as a result of the quantum tunneling of electrons in which electrons may pass through a barrier without expending sufficient energy. Before breakdown, the current in the gap between electrodes is very low. However, once the breakdown voltage is applied the electrical discharge leads to current spikes.

Although microscale discharge has been studied experimentally for more than a decade, our understanding of the fundamental physics is still limited due to the challenges in

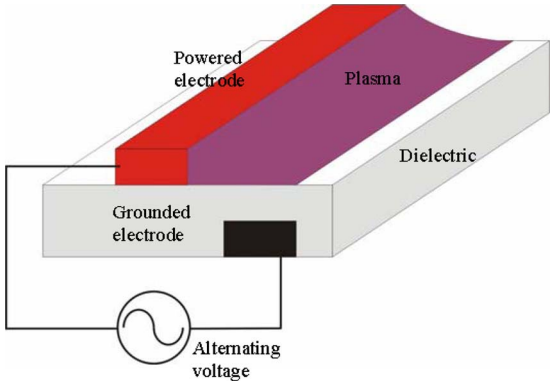

FIG. 1. (Color online) Schematic of rf DBD actuator for asymmetric configuration.

[a)]Electronic mail: roy@ufl.edu.

reduced length scales, unsteady phenomena, and rapid collisional interaction in microgaps. Therefore, numerical simulation is a possible remedy to overcome the experimental challenges.

In past few years, several numerical investigations of microscale discharge have been documented in the published literature. There are three basic models that describe the evolution of charged particles in plasma discharges. The first one is the hydrodynamic model,[9–11] which is the most popular. The second one is the kinetic model, which is the particle-in-cell/Monte Carlo collision (PIC/MCC) model.[12–14] The third one is the hybrid kinetic-fluid simulation model,[15,16] which is often used for modeling high-density plasma reactors. Kushner[9] presented a two-dimensional plasma hydrodynamic model of microscale discharge devices operating at pressures of 450–1000 Torr and dimensions of 15–40 μm. He found that such devices typically require more applied voltages to operate at lower pressures and because of this, they resemble discharges obeying Paschen's curve for breakdown. Boeuf *et al.*[10] utilized a fluid-based model to explain the physical mechanisms occurring in microhollow cathode discharges. Wang *et al.*[11] simulated a microscale discharge in helium at atmospheric pressure based on the hydrodynamic model and found that it resembled a macroscopic low pressure dc glow discharge in many respects.

A one-dimensional PIC-MCC model was developed by Choi *et al.*[12] for current-driven atmospheric-pressure helium microscale discharge. The PIC-MCC simulation results were compared with the hydrodynamic model results. The results showed the sheath widths were comparable between the PIC-MCC (Ref. 12) and the hydrodynamic model simulation,[11] and the peaks of the electron and ion densities were within the same orders of magnitude. However, the density profiles were significantly different. Radjenovic *et al.*[13] utilized the PIC-MCC model and found the deviation from Paschen's law when the gap between electrodes was smaller than 5 μm. They conjectured that because the electron mean free path was of the order of a few micrometers at atmospheric pressure, the electrical breakdown was initiated by the secondary emission processes instead of a gas avalanche process at small interelectrode spacing.

The third approach to simulate microscale plasma discharge is using the hybrid kinetic-fluid model. In this model the reaction rates are obtained by solving a basic Boltzmann equation, while the transport of electrons, ions, and neutrals is carried out via fluid models. Farouk *et al.*[15] simulated a dc argon microglow-discharge at atmospheric pressure for a pin-plate electrode configuration with interelectrode gap spacing of 200 μm together with an external circuit. The temperature measurements, which were around 500 K, suggested the discharge as a nonthermal, nonequilibrium plasma. The measured and predicted temperatures were found to compare favorably.

In this paper, we choose hydrodynamic plasma model due to its advantage of capturing reasonable physics of the microscale discharge at relatively low computational cost. First, we simulate a two-dimensional microscale volume discharge for a working gas of atmospheric nitrogen based on a self-consistent model of charged and neutral particles. Numerical results are then compared with previously reported experimental data. We conduct an error analysis for such volume discharge to benchmark the accuracy of the microscale plasma model. Finally, we implement the same model to self-consistently simulate the plasma-gas interactions of a first generation plasma micropump.

II. MODEL DETAILS

A hydrodynamic plasma model is utilized from Kumar and Roy[17] for multiscale plasma discharge simulation at atmospheric pressure. The model uses an efficient finite element algorithm anchored in the multiscale ionized gas (MIG) flow code.[3,17] The unsteady transport for electrons and ions is derived from conservation laws in the form of mass conservation equation. The species momentum is modeled using the drift-diffusion approximation under isothermal condition that can be derived from the hydrodynamic equation. At atmospheric pressure, the drift-diffusion approximation is reasonable and computationally efficient. The continuity equations for ion and electron number densities are given by:

$$\frac{\partial n_\alpha}{\partial t} + \frac{\partial (n_\alpha V_{\alpha j})}{\partial x_j} = \beta |\Gamma_e| - r n_i n_e, \quad \text{for} \quad \alpha = e, i, \quad \text{and} \quad j = 1,2, \tag{1}$$

where n is the number density, V is the species hydrodynamic velocity, r is the electron-ion recombination rate, subscript j is the flow direction of x and y, and subscript i and e are ion and electron, respectively. The working gas is nitrogen at 760 Torr. We use the value of r given by Kossyi *et al.*[18] The discharge is maintained using a Townsend ionization scheme. The ionization rate is expressed as a function of effective electron flux $|\Gamma_e|$ and Townsend coefficient β:

$$\beta = A p e^{-B/(|E|/p)}, \quad |\Gamma_e| = \sqrt{(n_e V_e)_x^2 + (n_e V_e)_y^2}, \tag{2}$$

where A and B are pre-exponential and exponential constants, respectively, p is the gas pressure, and E is the electric field, i.e., $E = -\nabla \varphi$. The ionic and electronic fluxes in Eq. (1) are written as:

$$n_i V_{ij} = n_i \mu_i (E + V_{ij} \times B_z) - D_i \frac{\partial n_i}{\partial x_j}, \tag{3}$$

$$n_e V_{ej} = -n_e \mu_e (E + V_{ej} \times B_z) - D_e \frac{\partial n_e}{\partial x_j}, \tag{4}$$

where the Lorentz force term, $\mathbf{V} \times \mathbf{B}$, brings in the effect of the magnetic field. We neglect the magnetic field effect for our problem. After some algebraic manipulations, we end up with the following equations:

$$\frac{\partial n_i}{\partial t} + \frac{\partial}{\partial x_j}\left\{ n_i \mu_i E_{x_j} - D_i \frac{\partial n_i}{\partial x_j} \right\} = \beta |\Gamma_e| - r n_i n_e, \tag{5}$$

$$\frac{\partial n_e}{\partial t} + \frac{\partial}{\partial x_j}\left\{ -n_e \mu_e E_{x_j} - D_e \frac{\partial n_e}{\partial x_j} \right\} = \beta |\Gamma_e| - r n_i n_e, \tag{6}$$

where μ is the mobility and D_e is the electron diffusion calculated from the Einstein relation, which is a function of the mobility μ_e, Boltzmann's constant k_B, and the electron

temperature, i.e., $D_e=\mu_e k_B T_e/e$. The ion mobility μ_i is expressed as a function of a reduced field (E/p).

The relation between electric field and charge separation is given by the Poisson equation:

$$\nabla \cdot (\varepsilon E) = q, \tag{7}$$

where ε is the dielectric constant, the net space charge $q=e(n_i-n_e)$, and e is the elementary charge.

The system of Eqs. (5)–(7) is normalized using the following normalization scheme: $\tau=t/t_0$, $z_j=x_j/d$, $N_e=n_e/n_0$, $N_i=n_i/n_0$, $u_{ej}=V_{ej}/V_B$, $u_{ij}=V_{ij}/V_B$, and $\phi=e\varphi/k_B T_e$ where V_B is the Bohm velocity, $V_B=\sqrt{k_B T_e/m_i}$, reference length d, which is usually a domain characteristic length in the geometry, the reference time $t_0=10^{-9}$ s, and reference density $n_0=10^{17}$ m^{-3} for weakly ionized gas.

In microscale flows, Knudsen number (Kn) is an important dimensionless parameter that determines the validity of continuum model for different regimes of fluid flow.[19] The Kn is defined as the ratio of the fluid mean free path λ and macroscopic characteristic length Λ, i.e., $\mathrm{Kn}=\lambda/\Lambda$. As Kn increases up to 10^{-3}, the no-slip boundary condition no longer applies. For the flow problem in microscale pump, the Kn is 2.6×10^{-4} assuring continuum flow with no-slip wall boundary condition. For a globally incompressible nitrogen gas (Mach number less than 0.3), the continuity and momentum equations are:

$$\frac{\partial V_{fj}}{\partial x_j} = 0, \tag{8}$$

$$\frac{\partial V_{fj}}{\partial t} + V_{fl}\frac{\partial V_{fj}}{\partial x_l} = \frac{qE_j}{\rho} - \frac{1}{\rho}\frac{\partial p}{\partial x_j} + \frac{\mu}{\rho}\frac{\partial^2 V_{fj}}{\partial x_l^2}, \tag{9}$$

where subscript f denotes the working fluid with bulk density ρ and bulk viscosity μ, and qE_j is the electrodynamic body force calculated from solving the plasma Eqs. (5)–(7).

III. FINITE ELEMENT METHOD WITH MIG

The finite element method (FEM) is a popular technique used for solving partial differential equations (PDE). The FEM is based on the Galerkin Weak Statement (GWS) and approximate the solution of the PDE. In the FEM, the global domain is divided in several elements, and the solution in each element is constructed from the basis function. The FEM has several advantages, such as easy to implement with complicated Neumann (flux) or Robin (convection) boundary conditions. The fundamental principle of the FEM is the construction of a solution approximation. Any real world problem distributed over a domain x_j can be approximated as a Taylor series of known coefficients a_i and functions $\psi_i(x_j)$:

$$L(\boldsymbol{\nu}) = \sum_i a_i \psi_i(x_j). \tag{10}$$

The plasma governing Eqs. (5)–(7) or fluid Eqs. (8) and (9) can be written generally as $L(\boldsymbol{\nu})=0$ where $\boldsymbol{\nu}$ is the vector containing N_i, N_e, and ϕ or V_j and p. The GWS approach requires that the measure of the approximation error should vanish in an overall integrated sense.[20,21] This gives a mathematical expression for the minimization of the weighted residual over the domain:

$$\mathrm{GWS} = \int_\Omega w L(\boldsymbol{\nu}) d\Omega = 0, \tag{11}$$

where Ω is the domain and w is the weighted basis function chosen to be a Strum–Louville function for orthogonality.

The MIG flow code is modular and anchored in the FEM. It has been developed and verified with one-, two-, and three-dimensional problems, including fluid dynamics and heat transfer related problems, micro/nanoscale flow, specifically to modeling dc/rf induced DBDs, and designing electromagnetic propulsion thrusters. Computed solutions show details of the distribution of charged and neutral particles and their effects on the flow dynamics for the various applications.[3,17,19,22]

MIG flow code employ the Newton–Raphson scheme for dealing with nonlinear terms. To solve the global sparse matrix, we apply an iterative sparse matrix solver called generalized minimal residual. The Newton–Raphson iteration for nonlinear solver is considered converged at any given time step when the L_2 norms of all the normalized solution variables and residuals are below a chosen convergence criterion of 10^{-5}.

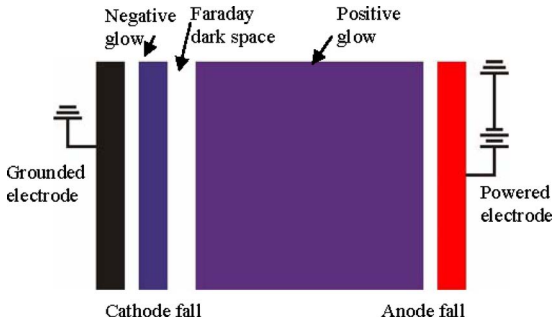

FIG. 2. (Color online) Schematic representation of various glows with dc discharge.

IV. PROBLEM DESCRIPTIONS

A. DC volume discharge

A direct current (dc) discharge forms plasma, sustained by a dc through an ionized medium shown in Fig. 2. A high voltage difference between electrodes results in the electrical breakdown of the gas. These discharges are characterized by continuous steady currents and are mostly sustained by secondary emissions.

We study a two-dimensional parallel plate dc volume discharge with microgaps varied from 200 to 5 μm at atmospheric pressure. The working gas is nitrogen (N_2), and the discharge is driven by a voltage of 500 V shown in Fig. 3(a). The computational grid consists of 25×30 biased biquadratic (nine-node) quadrilateral elements with the first node 0.1 μm away from the wall as shown in Fig. 3(b). We neglect the thickness of electrodes at the top and bottom surface. An electrode potential of 500 V is applied through an external circuit. The anode is at $y=0$, while the cathode is at

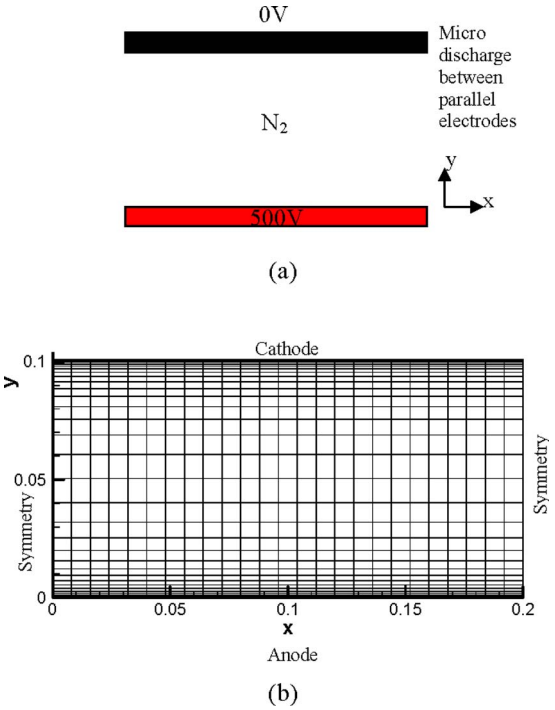

FIG. 3. (Color online) (a) Schematic of two-dimensional microscale volume discharge with nitrogen gas. (b) Computational mesh with 3111 nodes and 750 elements.

$y=0.1$. A vanishing ion density is imposed at the anode, while the electron density at the cathode is calculated from the flux balance using a secondary-emission coefficient of 0.1. The left and right boundaries of the computational domain are maintained at symmetry conditions. Initial distributions of electrons and ions are based on the dc sheath solution.[22] A uniform time step of 10^{-12} s is used for the time integration.

B. Plasma micropump

For the second case, we simulate plasma-gas interactions inside a cross section of plasma micropump.[23] Figure 4 shows the plasma micropump with four pairs of DBD actuators at both inlets and two pairs of DBD actuators at the center of the pump. The pump inlet openings are 250 μm at both sides and the single outlet opening is 500 μm at the top. Figure 5(a) shows the configuration of DBD actuator. The powered electrode is 20 μm wide, while the grounded electrode is 40 μm wide. The gap between electrodes is 10 μm at streamwise direction and 50 μm in vertical direction. Figure 5(b) shows two-dimensional computational

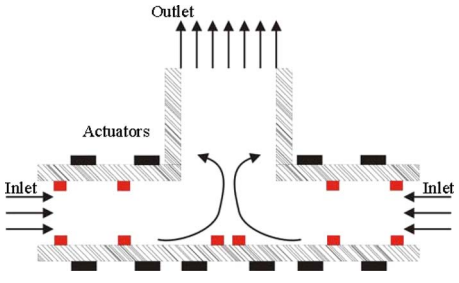

FIG. 4. (Color online) Schematic of microplasma pump.

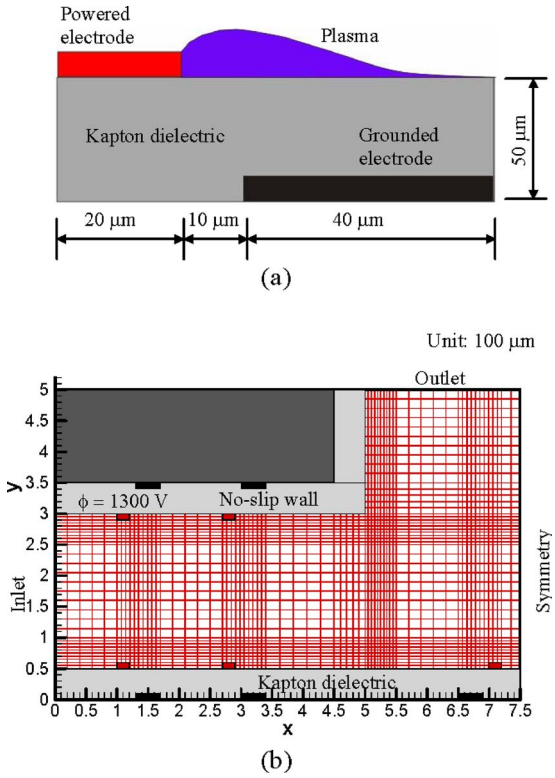

FIG. 5. (Color online) (a) Schematics of microscale plasma actuator. (b) Computational mesh with 13635 nodes and 3350 elements.

mesh for simulation of microplasma pump with a Kapton polyimide insulator, i.e., dielectric constant $\varepsilon_d=4.5\varepsilon_0$, where ε_0 is permittivity of vacuum. We simulate half of microplasma pump due to the symmetric configuration. The computational mesh consists of 67×50 elements and 13 635 nodes. The boundary condition of potential ϕ is equal to 1300 V. We neglect the thickness of powered electrode (at $y=0.5$ and 3) and grounded electrode (at $y=0$ and 3.5). For the flow simulation, gauge pressure is equal to zero at the inlet and the outlet. The right boundary is maintained as symmetry, and based on low Kn ($<10^{-3}$) all the dielectric surfaces are maintained at zero wall velocity.

V. RESULTS AND DISCUSSIONS

A. DC volume discharge

The simulation results for ion and electron densities along y-direction with various gaps from $d=200$ to 10 μm at atmospheric pressure (760 Torr) are presented in Fig. 6. The variables for y, N_e, and N_i were normalized using the following normalization scheme: $y=d/pl$, $N_e=n_e/n_0$, and $N_i=n_i/n_0$ where reference length pl varied from 2000 to 100 μm, and reference density $n_0=10^{17}$ m^{-3}. By decreasing the gap d, the sheath became more dominant to the plasma region. The location of the sheath was roughly at the bifurcation of ion and electron densities. The sheath thickness was a few Debye lengths based on the pressure, and Debye shielding confined the potential variation shown in Fig. 7. The function of a sheath is to form a potential barrier so that more electrons are repelled electrostatically. The potential lines are bent toward the cathode due to a very low density

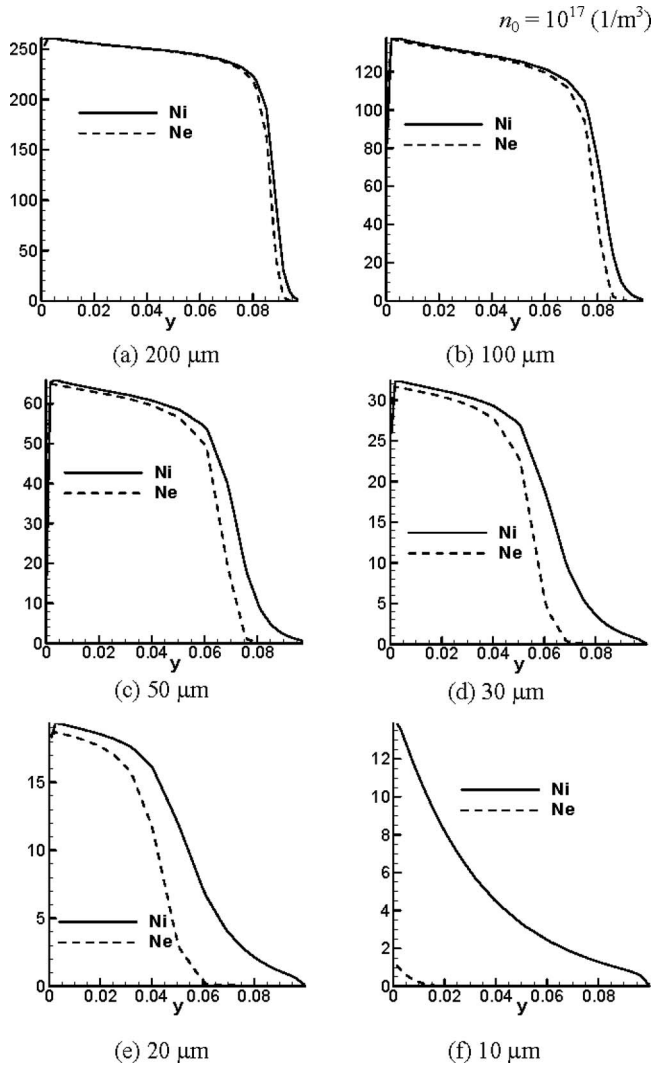

FIG. 6. (Color online) Ion (N_i) and electron (N_e) density distribution along y-direction with various gaps from d=200 to 10 μm. Reference density n_0=10^{17} m^{-3}.

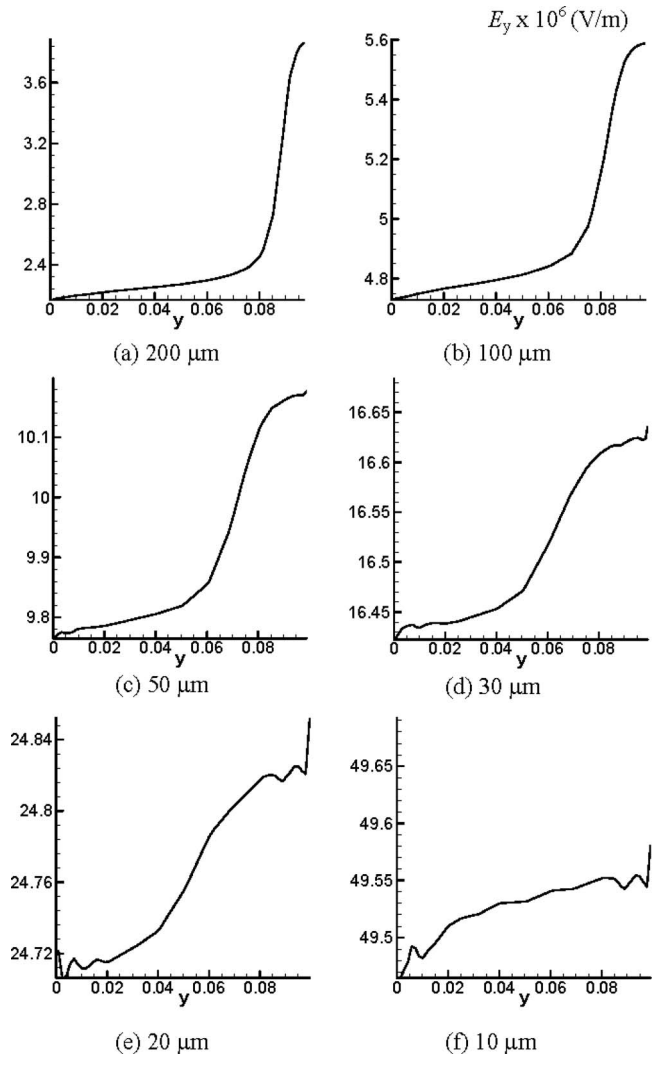

FIG. 7. (Color online) Electric field E_y (V/m) along y-direction with various gap from d=200 to 10 μm.

of electrons. This high potential will also drive electrons away from the cathode and form a cathode sheath thickness.

According to the order of accuracy of Newton–Raphson scheme for the nonlinear system of equations, the ideal convergence was quadratic convergence. However, Fig. 8 shows the convergence was between linear and quadratic because of linearization of the Jacobian matrix for numerical efficiency. The convergence is below 10^{-5} for every time step. Figure 9 shows that the computed electric field compared with the published experimental data of Longwitz[24] with a very good agreement from 50 to 5 μm interelectrode gaps. The computed charge density q slightly decreased as the gap d decreased, but it increased at the gap below 10 μm because much less electrons exist in the plasma region. Based on the calculation of the electric force (qE), we can see the force F_y is 1 MN/m^3 at 20 μm gap. Note that such force density is three orders of magnitude higher than that of macroplasma actuators. As the gap decreases the force seems to increase sharply. For example, at 5 μm gap the force density increases approximately sevenfold to 6.8 MN/m^3.

B. Plasma micropump

Figures 10(a)–10(c) plot the contour of potential (ϕ), ion number density (N_i), and electron number density (N_e). Fig-

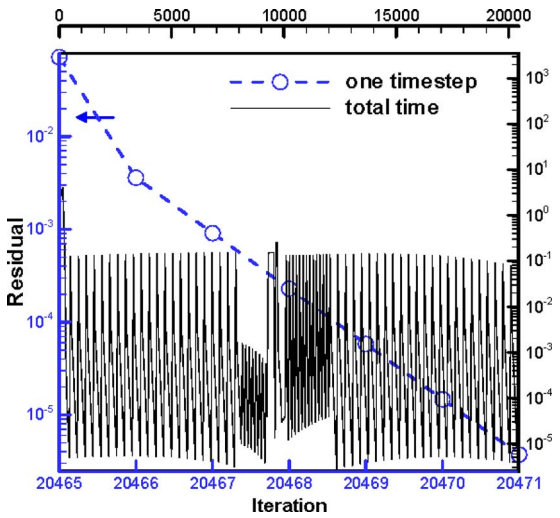

FIG. 8. (Color online) Convergence for one time step (iteration from 20 465 to 20 471) and total time steps (iteration from 0 to 20 471).

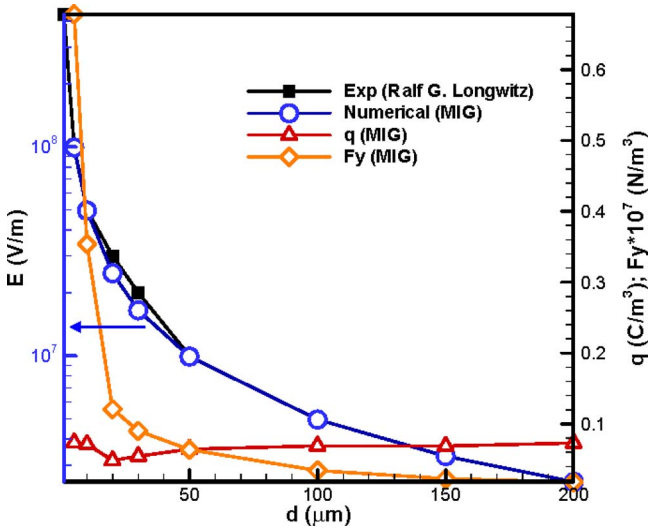

FIG. 9. (Color online) Comparison of numerical results and experimental data for electric field strength from $d=5$ to 50 μm. The charge density (q) and the electric force (F_y) are calculated from numerical results.

ure 10(a) shows an applied potential of 1300 V on the powered electrode (red). The electric field lines are acting from the powered electrode to the grounded electrode. Due to a large difference of potential between electrodes, the fluid is ionized at local regions shown in Figs. 10(b) and 10(c). We can see the net charge densities are concentrated inside the boundary layer near the wall, and it is almost zero away from the wall. Note that the charge densities depositing on the dielectric surface will cause a net electric force in the direction from the powered electrode to the grounded electrode. Therefore, outside the plasma region, the flow is mainly driven by viscous force.

The advantage of plasma micropump is to push the flow continuously without intermittent pulsed. Also, it can avoid the wear of the parts because there is no moving part inside the micropump. Figure 11(a) shows the flow behavior inside the plasma micropump. We can see the plasma drives the fluid into the pump at the inlet due to the net near-wall jet created by DBD actuators. We can also see one of the DBD actuators at right boundary (symmetry) with different configurations. This actuator is used for altering the fluid flow direction from horizontal to vertical direction and pushes the fluid upward to the outlet. However, it also creates a strong vortical structure inside the pump that will influence the mass flow rate of plasma micropump due to the energy loss. Figure 11(b) shows the V velocity distribution along x-direction normal to the outlet. The V velocity increases sharply from the wall (at $x=0.0005$ m) and becomes flat $V_{max}=3.1$ m/s at middle of the pump (at $x=0.000\,75$ m). Note that despite three orders of magnitude higher thrust density the net inducement of the air flow in these microactuators is similar to that of a standard macroscale plasma actuator. This is because the area in which these microactuators are in contact with air is also orders of magnitude smaller than their traditional counterparts. After simple calculation, we find the maximum flow rate $Q_{max}=46.5$ ml/min, which is a function of operating voltage of 1300 V for plasma micropump with nitrogen as working gas.

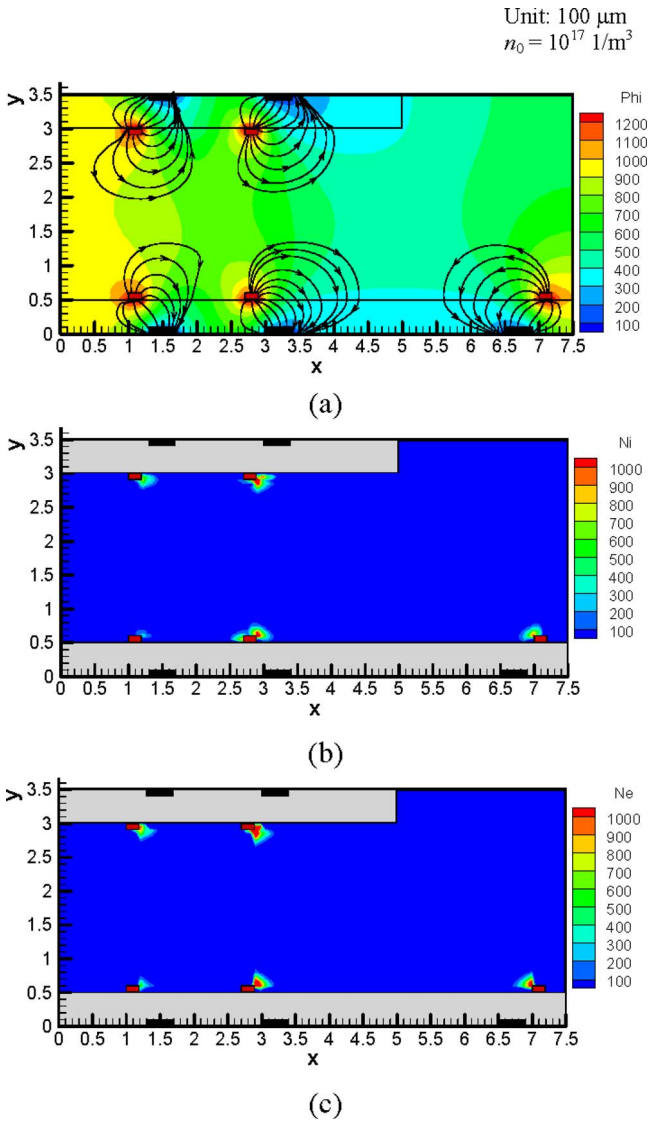

FIG. 10. (Color online) (a) Potential (ϕ) distribution with electric potential lines. (b) Ion number density (N_i) contour. (c) Electron number density (N_e) contour.

Such flow rate may be useful for the application of biological sterilization and decontamination, micropropulsions, and cooling of microelectronic devices.[25]

VI. CONCLUSIONS

Plasma actuation at atmospheric pressure is getting more attention in aerodynamics applications. To understand the effects of discharge in the fluid region, we solve system of plasma and Navier–Stokes equations based on the first-principles approach. The primary weakness of DBD actuators is the relatively small actuation effect as characterized by the induced flow velocity. In order to enhance the electric force for real aerodynamics applications, we study plasma discharge in microscale. First, a two-dimensional nitrogen volume discharge under applied dc potential has been modeled. It is based on first-principles using a self-consistent coupled system of hydrodynamic equations and Poisson equation. Two distinct regions may be observed, the quasi-neutral plasma where $N_i \approx N_e$ and the layer of sheath, which

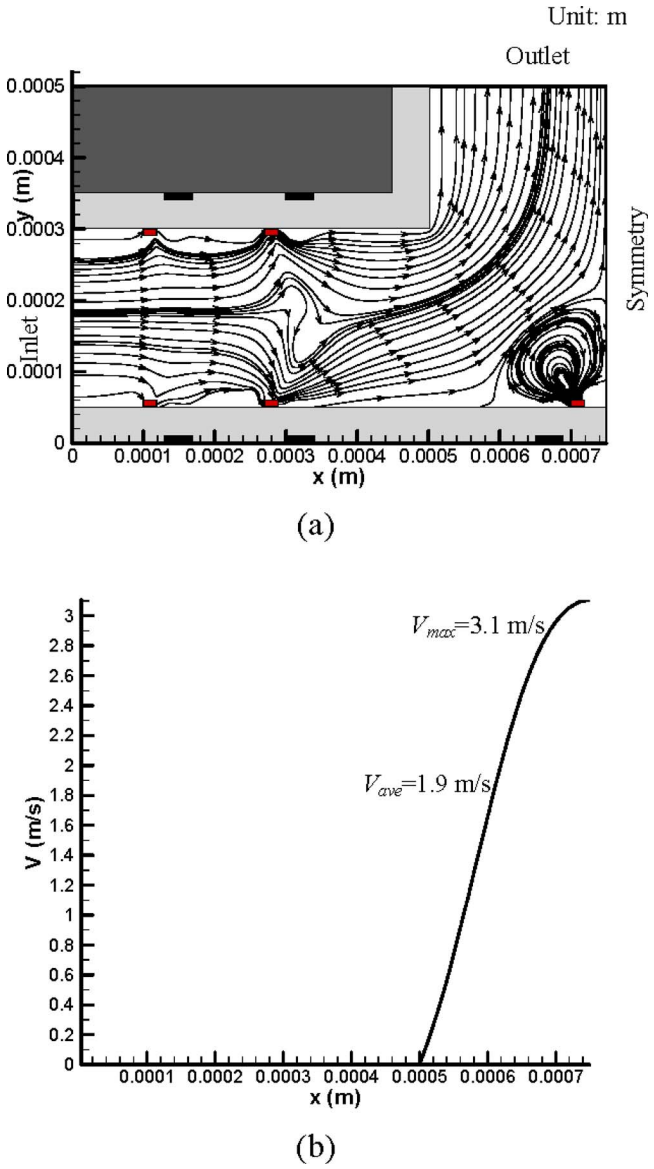

FIG. 11. (Color online) (a) The velocity stream traces inside the microplasma pump. (b) V velocity component distribution normal to the outlet.

is of several Debye lengths attached to the cathode where $N_i \gg N_e$. We can see the electron density in the sheath close to zero and the electric field arises out of this charge separation. As one approaches the sheath edge, there is an abrupt drop in the charge difference within a small spatial extent. This is the region of presheath where separation in ion and electron density curves begins and where electron density is much less than ion density. By decreasing the gap d, the sheath becomes more dominant to the plasma region. The results of electric field match well with published experimental data. Subsequently, we investigate a novel plasma micropump using the same microscale hydrodynamic plasma model. We find the air flow rate is around 46.5 ml/min for plasmamicro pump. Such plasma micropumps may become useful in a wide range of applications from microbiology to space exploration and cooling of microelectronic devices.

[1]J. R. Roth, Phys. Plasmas **10**, 2117 (2003).
[2]M. L. Post and T. C. Corke, AIAA J. **42**, 2177 (2004).
[3]D. V. Gaintonde, M. R. Visbal and S. Roy, 36th AIAA Plasmadynamics and Lasers Conference, AIAA 2005-5302, Toronto, Canada.
[4]K. H. Becker, K. H. Schoenbach, and J. G. Eden, J. Phys. D: Appl. Phys. **39**, R55 (2006).
[5]L. Baars-Hibbe, P. Sichler, C. Schrader, N. Lucas, K.-H. Gericke, and S. Buttgenbach, J. Phys. D: Appl. Phys. **38**, 510 (2005).
[6]T. Ono, D. Y. Sim, and M. Esashi, J. Micromech. Microeng. **10**, 445 (2000).
[7]J. M. Torres and R. S. Dhariwal, Nanotechnology **10**, 102 (1999).
[8]L. H. Germer, J. Appl. Phys. **30**, 46 (1959).
[9]M. J. Kushner, J. Appl. Phys. **95**, 846 (2004).
[10]J. P. Boeuf, L. C. Pitchford, and K. H. Schoenbach, Appl. Phys. Lett. **86**, 071501 (2005).
[11]Q. Wang, D. J. Economou, and V. M. Donnelly, J. Appl. Phys. **100**, 023301 (2006).
[12]J. Choi, F. Iza, J. K. Lee, and C. M. Ryu, IEEE Trans. Plasma Sci. **35**, 5 (2007).
[13]M. Radmilović-Radjenović, J. K. Lee, F. Iza, and G. Y. Park, J. Phys. D: Appl. Phys. **38**, 950 (2005).
[14]Z. L. Petrovic, S. Bzenic, J. Jovanovic, and S. Djurovic, J. Phys. D: Appl. Phys. **28**, 2287 (1995).
[15]T. Farouk, B. Farouk, D. Staack, A. Gutsol, and A. Fridman, Plasma Sources Sci. Technol. **15**, 676 (2006).
[16]T. J. Sommerer and M. J. Kushner, J. Appl. Phys. **71**, 1654 (1992).
[17]H. Kumar and S. Roy, Phys. Plasmas **12**, 093508 (2005).
[18]I. A. Kossyi, A. Y. Kostinsky, A. A. Matveyev, and V. P. Silakov, Plasma Sources Sci. Technol. **1**, 207 (1992).
[19]S. Roy, R. Raju, H. F. Chuang, B. A. Cruden, and M. Meyyappan, J. Appl. Phys. **93**, 8 (2003).
[20]A. J. Baker and D. W. Pepper, *Finite Element 1–2–3* (McGraw Hill, Columbus, 1991).
[21]G. F. Carey and J. T. Oden, *Finite Elements: A Second Course* (Prentice Hall, Englewood Cliffs, 1981), Vol. 2.
[22]S. Roy and D. Gaitonde, J. Appl. Phys. **96**, 2476 (2004).
[23]S. Roy, Method and apparatus for efficient micropumping, International Publication number PCT WO 2009/015371 (2007).
[24]R. G. Longwitz, "Study of gas ionization in a glow discharge and development of a microgas ionizer for gas detection and analysis," Ph. D. thesis, Institute of Microsystems and Microelectronics, Swiss Federal Institute of Technology, Lausanne, Switzerland, 2004.
[25]D. J. Laser and J. G. Santiago, J. Micromech. Microeng. **14**, R35 (2004).